

DR. RICHARD M LAINE (Orcid ID : 0000-0003-4939-3514)

DR. NATHAN J TAYLOR (Orcid ID : 0000-0003-4811-6558)

Article type : Article

Corresponding author email id: [talsdad@umich.edu](mailto:talsdad@umich.edu)

**Processing YAG/ $\alpha$ -Al<sub>2</sub>O<sub>3</sub> composites via reactive sintering Y<sub>2</sub>O<sub>3</sub>/Al<sub>2</sub>O<sub>3</sub> NP mixtures. A superior alternative to bottom up processing using atomically mixed YAlO<sub>x</sub> NPs.**

Richard M LAINE,\* Nathan J. TAYLOR and Sandra STANGELAND-MOLO

Dept of Materials Science and Engineering, University of Michigan

Ann Arbor, MI 48109-2136

**Abstract**

This effort contrasts “bottom-up” processing of YAG/ $\alpha$ -Al<sub>2</sub>O<sub>3</sub> composites where both elements (as 40-50 nm APSs nanopowders) are present at close to atomic mixing with reactive sintering where ball-milled mixtures of the individual nanopowders (40-50 nm APSs) give uniform elemental mixing at length scales closer to 100-800 nm with correspondingly much longer diffusion distances. In contrast to expectations, densification with control of final grain sizes is best effected using reactive sintering. Thus, reactive sintering to densities  $\geq 95\%$  occurs at only 1500 °C with final grain sizes of  $\approx 1000$  nm for all samples. In contrast “bottom up” processing to  $\geq 95\%$  densities is only achieved at 1600 °C, and with final grain sizes of 1700 nm. The reason for this unexpected behavior is that YAG phase forms early in the bottom up approach greatly inhib-

This is the author manuscript accepted for publication and has undergone full peer review but has not been through the copyediting, typesetting, pagination and proofreading process, which may lead to differences between this version and the [Version of Record](#). Please cite this article as [doi: 10.1111/jace.14980](https://doi.org/10.1111/jace.14980)

This article is protected by copyright. All rights reserved

iting diffusion promoted densification. In contrast, in reactive sintering, YAG is prevented from forming because of the longer diffusion distances such that densification occurs prior to full conversion of the  $Y_2O_3$  component to YAG. The found hardness values are statistically superior to literature values for composites near the known eutectic composition. In an accompanying paper, the addition of a third component reverses this behavior.

## Introduction

Traditional methods of processing composite ceramic materials can follow multiple pathways. The simplest being co-milling of desired components with proven dispersants and binders and thereafter casting and sintering monoliths targeting final densities > 95 % to ensure superior mechanical properties. While this approach often succeeds, it also can generate final products with large average grain sizes (AGSs > 5-10  $\mu\text{m}$ ) coincident with large critical flaws because of the high temperatures and/or long processing times required to achieve high final densities. This is especially true for efforts that explore the use of pressureless sintering.

Efforts to escape this demanding approach gave rise to chemical (sol-gel and polymer precursor) processing routes wherein atomic or near-atomic mixing of the target components was optimal.<sup>1,2</sup> The incentive was to minimize diffusion distances thereby minimizing processing times and/or temperatures, providing superior control of final densities, AGSs and therefore properties. Although this “bottom up” approach to processing works for multiple ceramic systems, it does not always work as we recently demonstrated.<sup>3,4</sup>

One clear impediment to its success arises when atomic mixing leads to very stable intermediate phases that resist further densification because of very low self-diffusion rates. Low diffusion rates thereby mandate higher sintering temperatures or longer times arriving at the same final AGSs and flaw size distributions as a traditional approach.

For example, the bottom up approach using single phase nanopowders (NPs) fails for atomically mixed  $Y_3Al_5O_{12}$  based ceramics because YAG exhibits very low diffusion rates. Such rates greatly inhibit further densification (Figure 1a) unless one resorts to much higher processing temperatures. Higher temperatures lead to excessive grain growth belying the utility of using bottom up NP processing.<sup>3</sup> In contrast, reactive sintering (Figure 1b) limits the rate of formation of YAG to later stages in the sintering process allowing full densification under much less demanding conditions giving finer control of final AGSs, flaw sizes and therefore properties.

**Insert Figure 1**

A second example explored phase segregation coincident with densification in spinel NPs of composition  $(\text{NiO})_{0.25}(\text{Al}_2\text{O}_3)_{0.75}$  targeting formation of  $(\text{NiAl}_2\text{O}_4)_{0.25}(\text{Al}_2\text{O}_3)_{0.50}$  composites. In this system, a comparison of the densification and final AGSs obtained at  $\approx 95\%$  density were identical to those obtained using mixtures of nano- $\text{NiAl}_2\text{O}_4$  spinel and nano- $\delta\text{-Al}_2\text{O}_3$ .<sup>4</sup> In this instance, the final target density mandated sintering conditions sufficient to drive extensive grain growth in the atomically mixed materials.

Thus it is of considerable importance to delineate the basic processes involved in phase separation and densification on sintering these NP systems. We present here the first of several papers targeting the elucidation of such processes with initial studies targeting fine-grained YAG/ $\alpha\text{-Al}_2\text{O}_3$  composites. This work serves as a prelude to developing thin films of the same or similar materials for structural applications but also for processing porous membranes for catalyst applications as suggested by Figures 2 and 3. These studies are enabled by using liquid feed-flame spray pyrolysis (LF-FSP) to produce a wide variety of single and mixed-metal oxide NPs in sufficient quantities ( $>30$  g/h) to allow extensive processing studies.

In the LF-FSP process metalloorganic precursors are dissolved in alcohols in the desired composition at 1-10 wt % ceramic loading and aerosolized with  $\text{O}_2$ .<sup>3-7</sup> Typical precursors include metal alkoxides, carboxylates, or  $\beta$ -diketonates. The aerosol is ignited using methane/ $\text{O}_2$  pilot torches generating flames at temperatures of 900-1500°C. The resultant gas phase species are rapidly ( $< 100$  ms) quenched forming NPs with compositions essentially identical to the precursor feed which are collected downstream in electrostatic precipitators.<sup>3-7</sup>

**Insert Figure 2**

**Insert Figure 3**

Rapid quenching generates atomically mixed NPs that are typically agglomerated but minimally aggregated with specific surface areas (SSAs) of 30-120  $\text{m}^2/\text{g}$  and average particle sizes (APSs) of 20-100 nm. In contrast to LF-FSP, other oxide NP synthesis methods such as coprecipitation and sol-gel processing often have lower degrees of mixing due to inhomogeneous rates of precipitation or hydrolysis, respectively.<sup>8</sup> LF-FSP is scalable and is well-studied.<sup>3-7,9,10</sup>

The YAG/ $\alpha\text{-Al}_2\text{O}_3$  composite system, especially the eutectic, shows promise as a high-temperature structural material in oxidizing environments.<sup>11-14</sup> A number of processing approaches to  $\text{Al}_2\text{O}_3$ -YAG (AY) composites have been used. Schehl et al. describe the utility of using yttrium alkoxide doping to pin exaggerated grain growth in  $\alpha\text{-Al}_2\text{O}_3$  through YAG phase

formation along grain boundaries.<sup>15</sup> The resultant micro/nano composites had well dispersed 200 nm YAG particles at  $\alpha$ -Al<sub>2</sub>O<sub>3</sub> grain boundaries. Sommer et al. produced 5, 10, and 15 vol% AY composites from both alkoxide coated Al<sub>2</sub>O<sub>3</sub> powders and mixtures of YAG and Al<sub>2</sub>O<sub>3</sub> NPs.<sup>16</sup> In their work, composites sintered at 1500° C for 3 h had theoretical densities that dropped from 98 to 94 %TD as YAG content increased from 5 to 20 vol %. Both approaches produced composites with grains in the 3-5  $\mu$ m size range.

Waku et al. synthesized eutectic composition, 45 vol% (80 mol%) AY composites from submicron Y<sub>2</sub>O<sub>3</sub> and  $\alpha$ -Al<sub>2</sub>O<sub>3</sub> powders.<sup>17</sup> These composites exhibited a sharp reduction in flexural strength above 1000° C, likely due to amorphous material at grain boundaries. Palmero et al. produced 50 vol% AY composites from NPs produced by the reverse-strike-precipitation method.<sup>18</sup> Mechanical activation of the reverse-strike powders by planetary milling gave powders that sintered to 98% theoretical density (TD) after 2 h at 1420° C with AGSs < 200 nm. No mechanical properties were reported.

## **Experimental**

### Materials.

Yttrium propionate was prepared by the dissolution of Y<sub>2</sub>(CO<sub>3</sub>)<sub>3</sub> or Y<sub>2</sub>O<sub>3</sub> (PIDC, Ann Arbor, MI) in propionic acid (Acros Organics, Geel, Belgium). Approximately 200 g (0.885 mol Y<sub>2</sub>O<sub>3</sub>) of starting material and 1 L (13.3 mol) of propionic acid was placed into a 3 L round bottom flask with magnetic stirring under dry N<sub>2</sub>. The reaction was heated to 120° C for 10 h, distilling off water. Full dissolution of the starting material into the propionic acid produces a yellow liquid, the reaction was then heated to 145° C to distill off excess acid. Care must be taken to ensure that some liquid remains at the end of the distillation or the product will decompose. The reaction was cooled, and yttrium propionate precipitated from the supersaturated solution. Typical ceramic yields determined by TGA for yttrium propionate used in the course of these studies were 34-37%, consistent with the 36.6 % theoretical ceramic yield for Y(O<sub>2</sub>CCH<sub>2</sub>CH<sub>3</sub>)<sub>3</sub>.

Alumatrane was used as the precursor to all Al<sub>2</sub>O<sub>3</sub> powders produced in the course of this study. Aluminum tri-*sec*-butoxide (870 g, 3.53 mol) was added to a 5 L mechanically stirred reactor under dry N<sub>2</sub> flow. Triethanolamine (631 g, 4.23 mol) was slowly added with an addition funnel. The reaction is exothermic, so triethanolamine was slowly added to maintain a temperature less than 80° C. The byproduct butanol was distilled off and the resulting viscous

alumatrane was dissolved in excess ethanol and the ceramic yield of the resulting solution was determined by TGA as described previously.<sup>7</sup>

### NP Synthesis

Precursors were dissolved in anhydrous ethanol (Decon Labs, King of Prussia, PA) and diluted to 1-5 wt % ceramic yield as measured by TGA. The precursor solutions are fed at 50-100 mL/min into an atomizing nozzle using O<sub>2</sub> at 80 psi and a flow rate of 3.5 mol/min. The atomized droplets are ignited by ceramic methane/O<sub>2</sub> torches 40 mm from the nozzle face. Four separate nozzles feed shield gas, which envelops the flame, providing mixing to the turbulent flame and ensuring complete combustion.<sup>3-7,10</sup>

NPs are drawn downstream of the combustion chamber by an exhaust system, providing 5-8 m<sup>3</sup>/min of exhaust. NPs entrained in the exhaust travel through two separate 120 cm aluminum tubes, which serve as electrostatic precipitators. Voltage is generated by a 10 kV AC oil burning furnace spark transformer. The output voltage is converted to DC with a custom bridge rectifier. Voltage is adjusted to provide maximum potential without arcing. Figure 4 provides a schematic of the flame spray pyrolysis apparatus.

**Figure 4.** General schematic of the flame spray pyrolysis apparatus.

NPs processed for compaction into ceramic bodies typically follow the following procedure. Approximately 10 g of as-produced NPs are ball milled with 2 wt% bicine in 300 mL of anhydrous ethanol with 0.5 mm yttrium stabilized ZrO<sub>2</sub>, 3 mm yttrium stabilized ZrO<sub>2</sub>, or 3 mm 99% Al<sub>2</sub>O<sub>3</sub> media for 24 hours. After 24 h of milling, the suspension is ultrasonicated for 20 minutes at 100 W using a Vibracell VC-505 ultrasonic horn (Sonics & Materials, Newtown, CT). The suspension is then allowed to settle for 24 h and decanted to remove large settled particles. The suspension is dried, ground, and sieved through 75 μm polypropylene mesh. The powder is redispersed in anhydrous ethanol with 4 wt % binder, typically polyethylene glycol (PEG) with a M<sub>w</sub> = 3400. The suspension is then ultrasonicated for 20 minutes at 100 W of power. The suspension is then dried, ground, and sieved through 20 μm polypropylene mesh.

### Pellet formation

Sieved powders are loaded into a 14.7 mm tungsten carbide die and pressed to 14 MPa for 3 min. to produce 700 to 1000 mg cylindrical pellets. Stearic acid is used as a die lubricant. Pellets are then vacuum sealed into latex gloves and cold isostatic pressed to in an Autoclave Engi-

neers CIP (Avure, Lewis Center, OH) to 200 MPa for 30 minutes. A typical pressure building and release rate is 10 MPa/min.

#### Thermal processing

Pellets are typically burned out 800 °C for 4 h in dry flowing air, with a ramp rate of 3 °C/min. Burnout and sintering up to 1100 °C is conducted in a BlueM (Thermo Fisher Scientific, Waltham, MA) tube furnace with a sealed quartz tube. Sintering from 1100-1500 °C is conducted in an MTI GSL-1600X (MTI Corporation, Richmond, CA) tube furnace. For sintering from 1500-1600 °C, a BlueM muffle furnace is used.

#### 2.4.1 Pellet densities

Pellets were first boiled for 4 h in deionized water, then were left for 24 h in room temperature water. Measurements were performed using an Archimedes density kit for an Ohaus Voyager Pro balance, with a sensitivity of 0.1 mg

#### Grain size measurements

Dense ceramic samples were polished with standard ceramographic techniques. Polished samples were thermally etched at a temperature 50° C under the sintering temperature for 30 minutes. ImageJ (NIH, Bethesda, MD) was used for grain size measurements. Two different grain size measurement techniques were used. For nanocomposite materials or composites with relatively simple grain size distributions, the lineal intercept method was used across greater than 500 grain intercepts on at least five images. For composites with differing grain size distributions, at least 250 grains of each material were measured in ImageJ and adjusted by a proportionality factor of 1.56 for random slices through tetradecahedron grains.

#### General characterization techniques

X-ray diffraction (XRD) was performed on a Rigaku rotating anode diffractometer (Rigaku USA, The Woodlands, TX) at 40 kV and 100 mA. Typical continuous scan ranges were from 10-70 ° 2 $\theta$  at 2°/min with a 0.02° interval. XRD patterns were analyzed using JADE 2010. Rietveld refinements were conducted within JADE using **the** XX peak fitting model.

Scanning electron microscopy (SEM) was performed using a FEI Nova Nanolab dualbeam SEM/FIB or FEI Quanta 200 SEM/FIB (FEI Corporation, Hillsboro, OR). Typical accelerating voltages were 5-20 kV, depending on sample conditions. Powder samples (50 mg) were

ultrasonicated in 20 mL of ethanol and dropped onto SEM sample stubs. Pellets were mounted on sample stubs with copper tape.

Transmission electron microscopy (TEM) was performed using a JEOL 3011 HREM (JEOL Ltd., Tokyo, Japan) at 300 kV. Powder (10 mg) was dispersed in 20 mL ethanol and wicked through a 400 mesh carbon coated copper grid.

Thermogravimetric analysis/differential thermal analysis (TGA/DTA) was performed on a TA Instruments Q600 TGA/SDT (TA Instruments, New Castle, DE). Precursor ceramic yields were determined by experimental runs at 10 °C/min to 1000 °C. Thermal behavior of ceramic particles or pellets was characterized by sample runs at 10 °C/min to 1400 °C. All experiments were performed with dry air flowing at 60 mL/min.

Surface area analyses were run on a ASAP 2020 sorption analyzer (Micromeritics, Norcross, GA). Samples were degassed for 8 h at 400 °C under vacuum. An 11 point BET method analysis was conducted on 200 mg samples at relative pressures of 0.05-0.35. Nitrogen was used as the adsorbate gas and analysis was conducted in liquid nitrogen. Average particle sizes (APSs) were derived from BET SSAs per the following, where  $\rho$  is the particle density.

Formula for particle size for spherical particles from SSA.

$$d = \frac{6}{(SSA) * \rho}$$

Dilatometry analyses were conducted using a Dilatronic II single pushrod dilatometer (Theta Industries, Port Washington, NY). Linear displacement was observed by a linear variable differential transformer (LVDT) and recorded by a custom LabView program. Constant heating rate experiments were conducted from room temperature to 1500 °C with a 10°C/min ramp rate in static air.

Vickers microhardness measurements were made using a Clark CM-400AT equipped for Vickers hardness measurements. All measurements were taken at a load of 500 g. Values given are an average of at least ten separate indentation sites.

Diffuse reflectance infrared Fourier transform spectroscopy (DRIFTS) samples were prepared by grinding 5 mg of NP with 400 mg of spectroscopy grade KBr. Samples were analyzed on a ThermoScientific Nicolet 6700 FTIR spectrometer (Thermo Fisher Scientific, Waltham, MA) under dry flowing nitrogen. Recorded spectra were an average of 60 scans at 400-4000  $\text{cm}^{-1}$  with a resolution of  $\pm 4 \text{ cm}^{-1}$ . A KBr blank was used as a reference sample.

## Results and discussion

An important aspect of working with NPs is the length scale of mixing. As-produced single-phase NPs will have atomic mixing and thus minimum diffusion lengths. Balling milling NPs does not provide sufficient energy to create new surfaces, thus primary particles sizes are not reduced. Ball milling does break up agglomerates, and in this case, only mixes the powders. If perfectly mixed, the length scale of mixing would be the distance between two adjacent nanoparticles of  $Y_2O_3$  and  $Al_2O_3$ . In practice, the length scale of homogeneous mixing provided by ball milling is *at least* the size of agglomerates that could be 100-800 nm in size. This is *at least two orders* of magnitude greater than atomically mixed NPs.

The major objective of the work reported here is to explore the utility of reactive sintering of mixtures of single oxide  $Y_2O_3$  and  $Al_2O_3$  NPs as a route to very fine-grained AY oxide composites and to compare this with a “bottom up” approach using nanocomposite, essentially atomically mixed  $YAlO_x$  NPs of the same composition and APS. The secondary objective is to determine the effect the length scale of mixing in the original NP compact has on the final composite microstructure and mechanical properties. Two-phase materials were produced from both LF-FSP NPs synthesized at the desired compositions and LF-FSP NPs of the constituent oxides mixed by ball milling to study the effects of phase development and sintering on the final microstructure. As seen in **Figure 1**, we find drastically different sintering behavior and final grain sizes in YAG tubes produced with these two processing techniques, which we mainly attribute to the differences in phase development due to the initial length scale of mixing.

### Powder characterization

Three atomically mixed compositions were synthesized resulting in powders with the BET SSAs and calculated APSs as well as those of the pure powders detailed in **Table 1**. The phase diagram **Figure S1** indicates that 88.5 mol %  $Al_2O_3$ - $Y_2O_3$  corresponds to the YAG/ $\alpha$ - $Al_2O_3$  eutectic at 45 vol%  $Al_2O_3$ , making it a popular composition in the literature for YAG/ $\alpha$ - $Al_2O_3$  composites. Although our processing conditions do not access the eutectic  $T_m$ , we processed several powder composites at this composition. The other two compositions synthesized here are ca.  $\pm 7$  mol% from this composition, and all three compositions are within the YAG/ $\alpha$ - $Al_2O_3$  two phase region.



Reactive sintering of  $Y_2O_3$  and  $Al_2O_3$  NPs will be referred to as the mixed nanoparticle approach. Sintering of LF-FSP nanoparticles produced at the exact composition will be referred to as the nanocomposite approach. To avoid confusion, we will refer to the samples by their composition in vol % and mol %  $Al_2O_3$  of the final composition. Both synthesis processes start from metastable states, so the final composition is used as the sample nomenclature to avoid confusion. As previously, we targeted densities 95 % theoretical density (TD) as a starting point for hot isostatic pressing (HIPing) for final densification with limited grain growth, if needed.

**Table 1.** Composition and BET SSAs for YAG- $Al_2O_3$  starting materials and composites.

NPs were synthesized under standard LF-FSP conditions. Figure 5 provides a SEM of 45 vol % (80 mol %)  $Al_2O_3$  as-produced nanocomposite NP, and is typical of all powders produced in this study. Particles are all generally < 100 nm, with no fraction of large particles present. Table 2 gives BET SSAs for powders produced in this study. APSs were calculated using  $\rho = 3.58$  g/cm<sup>3</sup>, representative of a low-density  $Al_2O_3$ - $Y_2O_3$  amorphous material since the true density of the powder is unknown, likely giving APSs slightly larger than their true values, as a low density would reflect a higher surface area for an equivalent mass.<sup>19</sup> BET derived APSs are within 20-50 nm, so the differences in particle size between nanocomposite nanoparticle and mixed nanoparticles are likely negligible.

#### Insert Figure 5

Figure 6 provides XRDs of as-produced nanocomposite powders. At 27 vol %  $Al_2O_3$ ,  $\delta$ - $Al_2O_3$ ,  $\delta^*$ - $Al_2O_3$ , and hexagonal  $YAlO_3$  are present, along with an amorphous hump centered at  $33^\circ 2\theta$ . Hexagonal  $YAlO_3$  is an intermediate phase, seen in almost all nano-YAG syntheses.<sup>20,21</sup>  $\delta$ - $Al_2O_3$  and  $\delta^*$ - $Al_2O_3$  are transition- $Al_2O_3$  phases, typical of nano- $Al_2O_3$ , and the two most common phases in LF-FSP  $Al_2O_3$ .<sup>7</sup> At 27 and 45 vol % (80 and 90 mol %)  $Al_2O_3$ ,  $\delta$ - $Al_2O_3$  is not seen, with only  $\delta^*$ - $Al_2O_3$  and hexagonal  $YAlO_3$  observed. Both retain a significant amorphous fraction, indicated by an amorphous hump centered at  $33^\circ 2\theta$ . Rietveld refinement of the XRD pattern for pure LF-FSP  $Y_2O_3$  powders used in this study gives 77% cubic and 23% monoclinic. XRD shows LF-FSP  $Al_2O_3$  to be a mixture of transition  $Al_2O_3$  phases, mostly  $\delta$  and  $\delta^*$ .

#### Insert Figure 6

#### Thermal analysis

**Figure 7** shows DTA traces from TGA/DTA analyses of pellets after binder burnout. Dotted traces correspond to the mixed NP approach, and solid lines to nanocomposite NPs. It is important to note that YAP or  $\text{YAlO}_3$  perovskite, and YAM, monoclinic  $\text{Y}_4\text{Al}_2\text{O}_9$ , are often intermediate products in YAG synthesis. Microdiffraction of TGA samples was used to identify the phase transformations associated with the exotherms. The increasing background for both 45 vol % (80 mol %)  $\text{Al}_2\text{O}_3$  samples are a function of DTA baseline calibration and do not indicate any real thermal affect.

Note that an additional slight exotherm appears in the 27 vol % DTA at 1240 °C. At present we cannot suggest a crystallization event that might cause this unless it is crystallization of  $\alpha\text{-Al}_2\text{O}_3$  which is in the region where such a crystallization might occur.<sup>4</sup>

#### Insert Figure 7

All three nanocomposite NP samples show an exotherm at  $\approx 935^\circ\text{C}$ , corresponding to the transformation from hexagonal  $\text{YAlO}_3$ ,  $\delta\text{-Al}_2\text{O}_3$ ,  $\delta^*\text{-Al}_2\text{O}_3$  to YAP and/or YAM as indicated by XRD. In the 27 vol % (66 mol %)  $\text{Al}_2\text{O}_3$  nanocomposite NP sample, an exotherm centered at  $1070^\circ\text{C}$  corresponds to the transformation to YAG. In the 45 vol % (80 mol %)  $\text{Al}_2\text{O}_3$  nanocomposite NP sample, an exotherm around  $1130^\circ\text{C}$  corresponds to either the YAG and/or  $\alpha\text{-Al}_2\text{O}_3$  transformation, as both phases are present by XRD after the exotherm. In the 64 vol % (90 mol %)  $\text{Al}_2\text{O}_3$  nanocomposite NP sample, an exotherm at  $1140^\circ\text{C}$  is typical of the transformation to  $\alpha\text{-Al}_2\text{O}_3$ , and the exotherm around  $1250^\circ\text{C}$  corresponds to the transformation to YAG from YAP/YAM and  $\text{Al}_2\text{O}_3$ . All three compositions show similar YAP/YAM transformation temperatures, but note that the YAG transformation is suppressed as  $\text{Al}_2\text{O}_3$  content increases. Per the phase diagram in **Figure S1** both YAP and YAM are  $\text{Y}_2\text{O}_3$  rich in comparison to YAG, so the transformation is diffusional. As  $\text{Al}_2\text{O}_3$  content increases, the local composition is more  $\text{Al}_2\text{O}_3$  rich, and the reaction to form YAG is delayed up to  $180^\circ\text{C}$  due the diffusion necessary for YAG transformation. Since YAG formation impedes further diffusion and densification, this late transformation benefits densification as seen in the dilatometry results.

There is no indication from the XRD data that YAM actually forms. However, it is possible that under the processing conditions some YAM forms during heating but it is likely transient unlike what we see in similar systems.<sup>3</sup> Thus, we cautiously imply in the above discussion that it may be present by writing YAP/YAM transition.

Alternately, the reduction in YAG transformation temperature as  $\text{Al}_2\text{O}_3$  increases suggests large YAP/YAM concentrations within a particle react with small amounts of  $\text{Al}_2\text{O}_3$  more quickly than small amounts of YAP/YAM react with large amounts of  $\text{Al}_2\text{O}_3$  to form YAG. This suggests a shift in the morphology of the particles as the composition is changed. Diffusional couples of  $\text{Y}_2\text{O}_3$  and  $\text{Al}_2\text{O}_3$  show the dominant mass transport is  $\text{Al}_2\text{O}_3$  diffusion into  $\text{Y}_2\text{O}_3$ , so small islands of  $\text{Al}_2\text{O}_3$  adjacent to YAP/YAM within a single particle may react more quickly to form YAG.<sup>21</sup> Hay studied YAG formation from diphasic  $\text{Y}_2\text{O}_3$ - $\text{Al}_2\text{O}_3$  gels and found diffusion of  $\text{Al}_2\text{O}_3$  is rate-controlling in YAG formation.<sup>22</sup> At high loadings of  $\text{Al}_2\text{O}_3$ , the  $\text{Al}_2\text{O}_3$  diffusion rate may be less than the diffusion rate into YAP/YAM, leading to the delay in YAG transformation seen here. Hay also observed the presence of YAG at temperatures as low as 800° C, indicating our DTA transformation temperatures are typical for this system.

In the mixed nanoparticle materials, an exotherm around 1160° C corresponds to the transformation to YAP, and the 1250-1270° C exotherm corresponds to the transformation to YAG, as seen by XRD, Figure 8. No change in thermal behavior is seen with compositional changes for

#### Insert Figure 8

the mixed NP processing approach. For mixed NPs, the reaction occurs as a diffusion couple between adjacent  $\text{Y}_2\text{O}_3$  and  $\text{Al}_2\text{O}_3$  NPs. The local  $\text{Y}_2\text{O}_3$ - $\text{Al}_2\text{O}_3$  interface is unchanged regardless of the global composition, so little change is seen in the DTA indicated phase transformations. In contrast, the local composition of the nanocomposite NPs closely matches the global composition. *This is an important observation because it indicates the length scale of mixing is approximately atomic vs the ball-milled NP samples.* As a result, the DTA indicates phase transformations are dependent on the global concentrations, basically indicating a “bulk property” effect.

#### Dilatometry

Figure 9 provides dilatometric traces for all three compositions from both nanocomposite and mixed NP samples. All samples had green densities of  $53 \pm 2\%$  TD. Both the mixed NP and nanocomposite 64 vol % (90 mol %)  $\text{Al}_2\text{O}_3$  composites show the most densification up to 1500° C at 15 and 14% linear strain, respectively. Both the 45 and 27 vol % (80 and 66 mol %)  $\text{Al}_2\text{O}_3$  mixed nanoparticle samples show similar densification levels of 12 and 13 % linear strain. The nanocomposite 45 and 27 vol %  $\text{Al}_2\text{O}_3$  samples show similar densification of  $\approx 8\%$  linear strain up to 1500° C, below that of their respective mixed-NP counterparts. The nanocomposite sin-

tering curves for 45 and 27 vol % (80 and 66 mol %)  $\text{Al}_2\text{O}_3$  are similar to pure LF-FSP YAG NPs.<sup>3</sup>

This may indicate once YAG is the volume majority phase, the sintering of the continuous 3D connected YAG grains may be rate limiting for composite densification. The sintering of the  $\text{Al}_2\text{O}_3$ -YAG composites reflects the dilatometry curves.

### Insert Figure 9

Final microstructure

Sintering efforts targeted densities of 95 % TD reflecting a practical density with closed porosity for further processing by HIPing to still higher densities with minimal grain growth. Different sintering temperatures were used, but the data here are presented as an iso-density case. **Figure 10** shows SEMs of polished and then thermally etched samples for all three compositions for both processing methods.

In a reflection of the higher densification at lower temperatures, the mixed nanoparticle composites sinter *to much finer grain sizes* than the nanocomposite nanoparticles at equivalent densities of  $95 \pm 1$  %TD. In general, the larger grain sizes observed for the nanocomposite NP case are likely a consequence of the higher sintering temperatures required. **Table 2** gives the measured AGSs from the polished SEM micrographs. AGSs do not differ significantly with composition. All of the mixed nanoparticle composites have average grain sizes for both phases of  $\approx 1000$  nm. The nanocomposite nanoparticle samples have grain sizes for both phases of  $\approx 1700$  nm.

### Insert Figure 10

**Table 2.** AGSs and hardnesses for three compositions (NN = nanocomposite, Mix = mixed NPs).

Vickers microhardness

Microhardness data for each sample are also tabulated in **Table 2**. Larrea et al. suggest that the  $\text{Al}_2\text{O}_3$  content dominates the hardness in YAG/ $\alpha$ - $\text{Al}_2\text{O}_3$  eutectic composites. Our results fit well with this observation.<sup>23</sup> Higher hardness values are observed as  $\text{Al}_2\text{O}_3$  volume fraction increases. No significant differences between the nanocomposite and mixed NP samples were observed. The hardness of bulk  $\text{Al}_2\text{O}_3$  is commonly cited as 17.7 GPa, but values as high as 20 GPa have been obtained from NP processed  $\text{Al}_2\text{O}_3$  with 1  $\mu\text{m}$  AGS.<sup>24</sup> The observed values sug-

gest that the critical flaw sizes in both types of materials are similar and *may be a consequence of sample polishing* (see work of Niihara et al)<sup>25</sup> rather than offering a direct measure of the effects of AGSs. Future studies will address this issue.

The bulk Al<sub>2</sub>O<sub>3</sub> hardness is equivalent to our 64 vol % (90 mol %) Al<sub>2</sub>O<sub>3</sub> mixed NP sample, and below the nanocomposite NP sample of the same composition, but both are below the 20 GPa for NP derived Al<sub>2</sub>O<sub>3</sub>. For reference, Li and Gao obtained a hardness of 16.15 GPa for 75 vol% Al<sub>2</sub>O<sub>3</sub>-YAG composites.<sup>26</sup> Although these results suggest enhanced hardness due to a pseudo-Hall-Petch grain size effect, the high hardness values here may also be a consequence of the low loading used in microhardness testing.<sup>27</sup> Our microhardness testing used a load of 500 g, whereas it has been suggested that Vickers hardness tests for true hardness should be run using 5-10 kg loads. Comparative hardness studies with higher loads will be performed in the future to determine if a true grain size hardness effect is present. Again an alternative interpretation is that the fatal flaws in both materials are a consequence of surface finish from polishing of the test samples.<sup>25</sup> This also will be tested in future studies.

The nanocomposite NP processing scheme prevents densification, and as a result mixed nanoparticle reactive sintering provides finer grain sizes in 95% dense composites at all compositions tested. In the YAG/ $\alpha$ -Al<sub>2</sub>O<sub>3</sub> system, the mixed NP case provides finer microstructures, with no indication that particle mixing affected the final phase dispersion. The AGSs are consistent with literature, except for Palmero et al.<sup>18</sup> who found < 200 nm AGSs from planetary milled powders. Although not well explored here, the finer grain sizes of the mixed NP samples may lead to superior mechanical properties both in bulk and in thin films, especially laminates.

## Conclusions

YAG/ $\alpha$ -Al<sub>2</sub>O<sub>3</sub> composites were prepared using two processing schemes, the mixing of the constituent oxide NPs, or mixed NPs, and single-phase NPs containing the overall stoichiometry of the composite. In all cases, the mixed NP cases sinter to microstructures with *significantly* finer grain sizes than found with nanocomposite NPs at equivalent densities. As in our earlier work,<sup>3,4</sup> transformation to the YAG phase prevents low temperature densification in the single-phase nanoparticle materials supporting the idea that *the bottom up approach is not always the best approach* to processing selected composite materials not just single-phase materials.

In nanocomposite NPs, DTA indicates a significant reduction in the YAG nucleation temperature from 1250° to 1070°C as Y<sub>2</sub>O<sub>3</sub> content increases. Since YAG forms by reaction of Al<sub>2</sub>O<sub>3</sub>

with YAP/YAM, this suggests the particle morphology offers smaller diffusion distances for rate-limiting  $\text{Al}_2\text{O}_3$  species as  $\text{Y}_2\text{O}_3$  content increases. In the mixed NP processing scheme, no change in the thermal behavior is seen with changing composition, consistent with a fixed reaction front between adjacent  $\text{Al}_2\text{O}_3$  and  $\text{Y}_2\text{O}_3$  nanoparticles.

Hardness testing showed no significant increase in the hardness between the nanocomposite and mixed NP processing schemes. Hardness did increase as the  $\text{Al}_2\text{O}_3$  volume fraction increased, to a peak of  $18.6 \pm 1.7$  GPa for the 64 vol%  $\text{Al}_2\text{O}_3$  nanocomposite NP sample. This value is above that of bulk  $\text{Al}_2\text{O}_3$ , but lower than that of some fine-grained  $\text{Al}_2\text{O}_3$ . Future testing with higher Vickers hardness loads should be performed to determine if we are seeing a true Hall-Petch type increase in hardness due to grain size.

These results are very important in processing fine-grained ceramic films given that finer grain sizes provide a more torturous path for crack propagation *if cracks propagate along grain boundaries*. An alternative explanation is that coincident with grain growth average flaw sizes also grow leading to poorer mechanical properties.

In terms of our long-term goals, finer grain sizes will also provide higher SSAs for porous membranes that can be used as catalyst support. In addition, finer grains in thin films provide flexibility suggesting superior mechanical properties as illustrated recently in our work on lithium ceramic electrolytes and nickel aluminate thin films.<sup>5,6,28-29</sup>

As we test the bottom-up approach to composite synthesis, we find mixed NP processing to be superior to the nanocomposite NP processing scheme. This runs contrary to the idea that controlling the composite composition at the finest possible length scale leads to the best composites. In addition, the results described here indicate powder processing is likely much more important the powder chemical homogeneity. Despite the advantage of the mixed nanoparticle approach, the AGSSs are around  $1 \mu\text{m}$ . To reduce the grain size into the nanometer range, we explored the addition of a third phase to both further pin grain boundary movement and provide lower temperature sintering. These studies are described elsewhere,<sup>30</sup> where we add a  $\text{Y}_2\text{O}_3$  stabilized  $\text{ZrO}_2$  phase to YAG/ $\alpha$ - $\text{Al}_2\text{O}_3$  composites.

## Acknowledgements

We are grateful for support of this work by NSF through DMR Grant 1105361.

## References

1. Brinker, C. J.; Scherer, G.; Sol-Gel Science, Academic Press, N.Y., N.Y. 1991.
2. Laine, R.M.; Sellinger, A.; "Si-containing ceramic precursors," in The Chemistry of Organic Silicon Compounds Vol. 2, Z. Rappoport Y. Apeloig, eds., J. Wiley & Sons Ltd. London, 1998, 2245-310.
3. Taylor, N. J.; Laine, R.M.; "Bottom up processing is not always optimal. YAG tubes," *Adv. Functional Mater.* 2014; 24: 1125-1132.
4. Taylor, N. J.; Pottebaum, A. J.; Uz, V.; Laine, R. M.; "The bottom up approach is not always the best processing method. Dense  $\alpha$ -Al<sub>2</sub>O<sub>3</sub>/NiAl<sub>2</sub>O<sub>4</sub> composites," *Adv. Functional Mater.* 2014; 24: 3392–3398.
5. Yi, E.; Wang, W.; Mohanty, S.; Kieffer, J.; Tamaki, R.; Laine, R. M.; "Materials that can replace liquid electrolytes in Li batteries: Superionic conductivities in Li<sub>1.7</sub>Al<sub>0.3</sub>Ti<sub>1.7</sub>Si<sub>0.4</sub>P<sub>2.6</sub>O<sub>12</sub>. Processing combustion synthesized nanopowders to free standing thin films," *J. Power Sources* 2014; 269: 577-588.
6. Yi, E. and Laine, R. M. unpublished work.
7. Hinklin, T.; Toury, B.; Gervais, C.; Babonneau, F.; Gislason, J. J.; Morton, R. W.; Laine, R. M.; "Liquid-Feed Flame Spray Pyrolysis of Metalloorganic and Inorganic Alumina Sources in the Production of Nanoalumina Powders," *Chem. Mater.*, 2004; 16: 21–30.
8. Kakihana, M. "Invited review 'sol-gel' preparation of high temperature superconducting oxides," *Journal of Sol-Gel Science and Technology*, 1996; 6: 7–55.
9. Pratsinis, S. E.; "Flame aerosol synthesis of ceramic powders," *Progress in Energy and Combustion Science*, 1998; 24:197–219.
10. Sutorik, A. C.; Laine, R. M.; Marchal, J. C.; Johns, T.; Hinklin, T.; "Mixed-metal oxide particles by liquid feed-flame spray pyrolysis of oxide precursors in oxygenated solvents," U.S. Patent 7220398 issued May 22, 2007.
11. Parthasarathy, T.A.; Mah, T.-II; Matson, L. E.; "Processing, structure and properties of alumina-YAG eutectic composites," *J. Ceram. Proc. Res.*, 2004; 5: 80-390.
12. Hirano, K.; "Application of eutectic composites to gas turbine system and fundamental fracture properties up to 1700 °C," *Journal of the European Ceramic Society*, 2005; 25: 1191–1199.

13. Waku, Y.; Nakagawa, N.; Wakamoto, T.; Ohtsubo, H.; Shimizu, K.; Kohtoku, Y.; "A ductile ceramic eutectic composite with high strength at 1,873 K," *Nature*, 1997; 389: 49–52.
14. LLorca, J.; Orera, V. M.; "Directionally solidified eutectic ceramic oxides," *Progress in Materials Science*, 2006; 51: 711–809.
15. Schehl, M.; Díaz, L. A.; Torrecillas, R.; "Alumina nanocomposites from powder–alkoxide mixtures," *Acta Materialia*, 2002; 50: 1125–1139.
16. Sommer, F.; Kern, F.; El-Maghraby, H. F.; El-Ezz, M. A.; Awaad, M.; Gadow, R.; Naga, S. M.; "Effect of preparation route on the properties of slip-casted Al<sub>2</sub>O<sub>3</sub>/YAG composites," *Ceramics International*, 2012; 38: 4819–4826.
17. Waku, Y.; Nakagawa, N.; Ohtsubo, H.; Mitani, A.; Shimizu, K.; "Fracture and deformation behaviour of melt growth composites at very high temperatures," *J. Mater. Sci.*, 2001; 36: 1585–1594.
18. Palmero, P.; Simone, A.; Esnouf, C.; Fantozzi, G.; Montanaro, L.; "Comparison among different sintering routes for preparing alumina-YAG nanocomposites," *J. Europ. Ceram. Soc.*, 2006; 26: 941–947.
19. Wilding, M. C.; Benmore, C. J.; McMillan, P. F.; "A neutron diffraction study of yttrium- and lanthanum-aluminate glasses," *J. Non-Crystalline Solids*, 2002; 297:143–155.
20. Sim, S.-M.; Keller, K. A.; Mah, T.-I.; "Phase formation in yttrium aluminum garnet powders synthesized by chemical methods," *J. Mater. Sci.*, 2000; 35: 713–717.
21. Glushkova, V. B.; Krzhizhanovskaya, V.A.; Egorova, O. N.; Udalov, Yu. P.; Kachalova, L. P.; "Interaction of Yttrium and Aluminum-Oxides," *Inorg. Mater.*, **19** 80-84 (1983).
22. Hay, R. S.; "Phase transformations and microstructure evolution in sol-gel derived yttrium-aluminum garnet films," *J. Mater. Res.*, 1993; 8 :578–604.
23. Larrea, A.; Orera, V. M.; Merino, R. I.; Peña, J. I.; "Microstructure and mechanical properties of Al<sub>2</sub>O<sub>3</sub>–YSZ and Al<sub>2</sub>O<sub>3</sub>–YAG directionally solidified eutectic plates," *J. Europ. Ceram. Soc.*, 2005; 25: 1419–1429.
24. Teng, X.; Liu, H.; Huang, C.; "Effect of Al<sub>2</sub>O<sub>3</sub> particle size on the mechanical properties of alumina-based ceramics," *Mater. Sci. Eng.: A*, 2007; 452–453: 545–551.
25. Ohji, T.; Jeong, Y.-K.; Choa, Y.-H.; Niihara, K.; "Strengthening and Toughening Mechanisms of Ceramic Nanocomposites," *J. Am. Ceram. Soc.*, 1998; 81: 1453–60 and references therein.



26. Li, W. Q.; Gao, L.; “Processing, microstructure and mechanical properties of 25 vol% YAG- $\text{Al}_2\text{O}_3$  nanocomposites,” *Nanostructured Mater.*, 1999; 11: 1073–1080.
27. A. Krell, “Comment: The Effect of Grain Size on the Mechanical and Optical Properties of Spark Plasma Sintering-Processed Magnesium Aluminate Spinel  $\text{MgAl}_2\text{O}_4$  (Rothaman et al.),” *Int. J. Appl. Ceram. Technol.*, 2015; 12: E174–E175.
28. Yi, E.; Wang, W.; Kieffer, J.; Laine, R. M.; “Key parameters governing the densification of cubic- $\text{Li}_7\text{La}_3\text{Zr}_2\text{O}_{12}$   $\text{Li}^+$  conductors,” *J. Power Sources*, 2017; 352:156-164.
29. Liang, B.; Yi, E.; Jia, D.; Zhou, Y.; Sato, T.; Noda, S.; Laine, R. M. “Liquid-Feed Flame Spray Derived  $[\text{NiO}]_{0.25}[\text{Al}_2\text{O}_3]_{0.75}$  and  $[\text{NiO}]_{0.50}[\text{Al}_2\text{O}_3]_{0.50}$  Nanopowders Are Easily Processed to Thin, Dense, Flexible  $\text{NiAl}_2\text{O}_4$ - $\text{Al}_2\text{O}_3$  and  $\text{Ni-Al}_2\text{O}_3$  Composite Film,” in preparation.
30. Taylor, N. J.; Stangeland-Molo, S.; Laine, R. M.; “Comparing bottom up processing with reactive sintering. Processing routes to dense  $\text{Al}_2\text{O}_3$ -YAG-YSZ composites from single and three-phase nanoparticles (NPs). Bottom up processing wins this time.” *J. Amer. Ceram. Soc.* 2017. DOI: 10.1111/jace.14761

### List of Figure captions

**Figure 1.** SEM of fracture surface of **a.**  $\text{Y}_3\text{Al}_5\text{O}_{12}$  nanocomposite composition (70 % dense); **b.** ball milled nano  $\text{Y}_2\text{O}_3$ - $\text{Al}_2\text{O}_3$  of same composition (>96 % dense): 2-step heated to 1500/1300°C.<sup>3</sup>

**Figure 2.** Sintering a  $\text{NiAl}_2\text{O}_4$ - $\text{Y}_2\text{O}_3$  film at 1400 °C/1 h/20 %  $\text{H}_2$ - $\text{N}_2$ . ( $\text{Ni } T_m = 1450$  °C) producing a porous YAG/Ni metal composite.<sup>6</sup>

**Figure 3.** XRD of Figure 2 film. Ni metal and YAG are main crystalline phases, suggesting  $\text{Al}_2\text{O}_3$  from spinel reacts with  $\text{Y}_2\text{O}_3$ . Small amount of  $\text{YAlO}_3$  observed due to off stoichiometry or incomplete reaction.<sup>6</sup>

**Figure 4.** General schematic of the flame spray pyrolysis apparatus.

**Figure 5.** SEM of as-produced 45 vol% (80 mol%)  $\text{Al}_2\text{O}_3$  nanocomposite nanoparticles.

**Figure 6.** XRDs for 27, 45, and 64 vol % (66, 80, and 90 mol %)  $\text{Al}_2\text{O}_3$  nanocomposite NPs.

**Figure 7.** DTA traces of both mixed nanoparticle (dotted lines) and nanocomposite nanoparticle pellets (solid lines). (P =  $\text{YAlO}_3$  perovskite, M =  $\text{Y}_4\text{Al}_2\text{O}_9$  monoclinic, YAG =  $\text{Y}_3\text{Al}_5\text{O}_{12}$ ,  $\alpha$  =  $\alpha\text{-Al}_2\text{O}_3$ ).

**Figure 8.** XRDs of 1:1 mixtures of  $\text{Y}_2\text{O}_3:\text{Al}_2\text{O}_3$  nanopowder pellets on sintering for 3 h/air at 800–1400 °C. Y =  $\text{Y}_2\text{O}_3$ , A = transition alumina, P =  $\text{YAlO}_3$ , M =  $\text{Y}_2\text{Al}_4\text{O}_9$ , G =  $\text{Y}_3\text{Al}_5\text{O}_{12}$  garnet.

**Figure 9.** Dilatometry traces for all compositions studied.

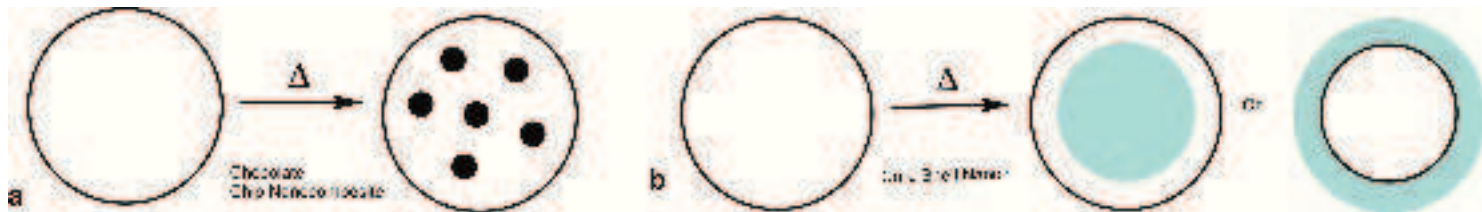
**Figure 10.** SEMs at 95 %TD for **a.** 64 vol%  $\text{Al}_2\text{O}_3$  nanocomposite **b.** 64 vol%  $\text{Al}_2\text{O}_3$  mixed **c.** 45 vol%  $\text{Al}_2\text{O}_3$  nanocomposite **d.** 45 vol%  $\text{Al}_2\text{O}_3$  mixed **e.** 27 vol%  $\text{Al}_2\text{O}_3$  nanocomposite **f.** 27 vol%  $\text{Al}_2\text{O}_3$  mixed.

mol% Y <sub>2</sub> O <sub>3</sub>	mol % Al <sub>2</sub> O <sub>3</sub>	mol % Al <sub>2</sub> O <sub>3</sub>	mol% YAG	wt% Al <sub>2</sub> O <sub>3</sub>	wt% YAG	vol% Al <sub>2</sub> O <sub>3</sub>	vol% YAG	BET m <sup>2</sup> /g	APSs nm
11.5	88.5	90.0	10.0	60.8	39.2	63.9	36.1	41	41
18.5	81.5	80.4	19.6	41.4	58.6	44.6	55.4	38	44
25.3	74.7	65.8	34.2	24.9	75.1	27.4	72.6	53	23
0	100							65	26
100	0							53	23

Author Manuscript

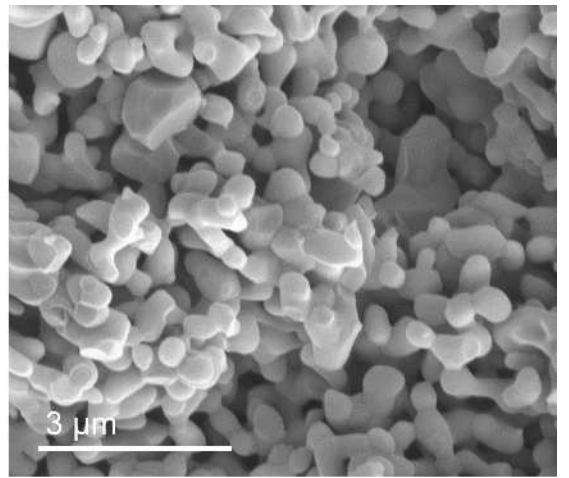
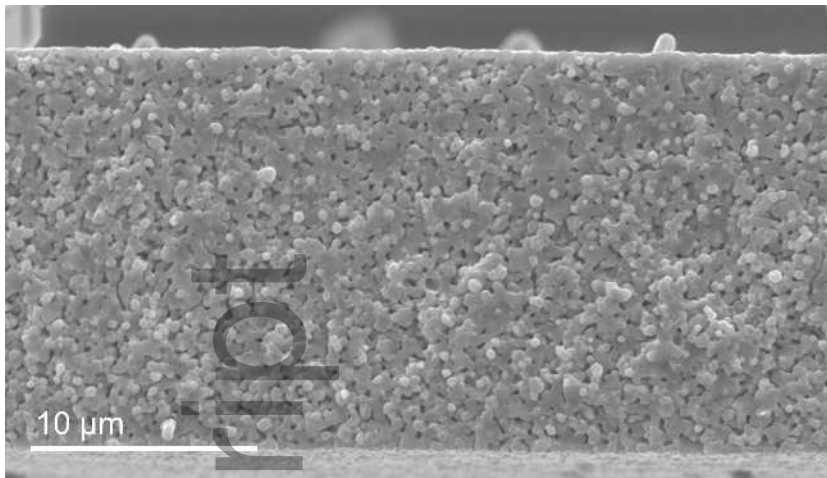
	YAG [nm]	Al <sub>2</sub> O <sub>3</sub> [nm]	%TD	Schedule	Hardness [GPA]
64 vol% Al <sub>2</sub> O <sub>3</sub> NN	1800 ± 310	1600 ± 400	95	1500 °C 8h	18.6 ± 1.7
64 vol% Al <sub>2</sub> O <sub>3</sub> Mix	730 ± 270	1100 ± 460	95	1500 °C 8h	17.8 ± 1.5
45 vol% Al <sub>2</sub> O <sub>3</sub> NN	1800 ± 370	1700 ± 300	94	1600 °C 4h	16.5 ± 1.7
45 vol% Al <sub>2</sub> O <sub>3</sub> Mix	980 ± 250	1000 ± 280	95	1600 °C 4h	16.5 ± 1.4
27 vol% Al <sub>2</sub> O <sub>3</sub> NN	1700 ± 420	1700 ± 380	95	1600 °C 4h	15.1 ± 1.3
27 vol% Al <sub>2</sub> O <sub>3</sub> Mix	910 ± 380	1000 ± 320	95	1500 °C 8h	14.7 ± 0.8

Author Manuscript



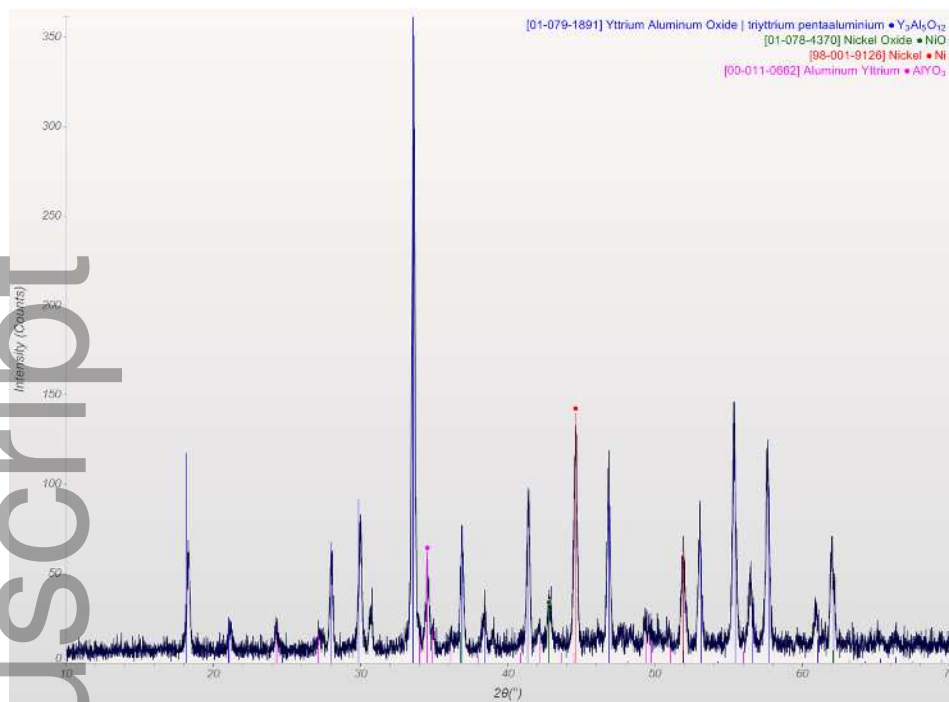
jace\_14980\_f1.tif

Author Manuscript

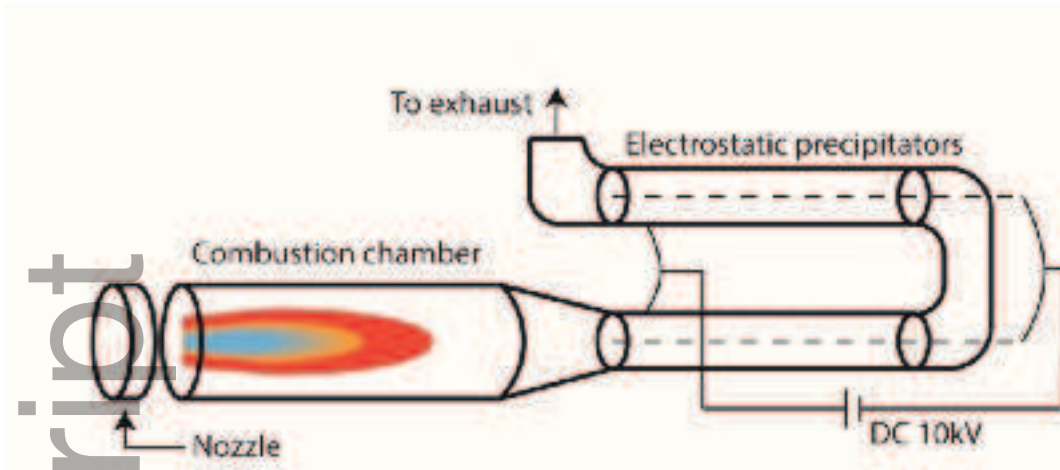


jace\_14980\_f2.tif

Author Manuscript



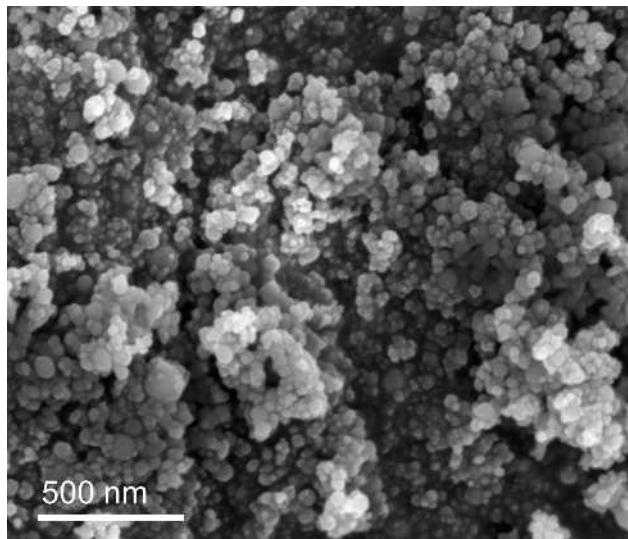
jace\_14980\_f3.tif



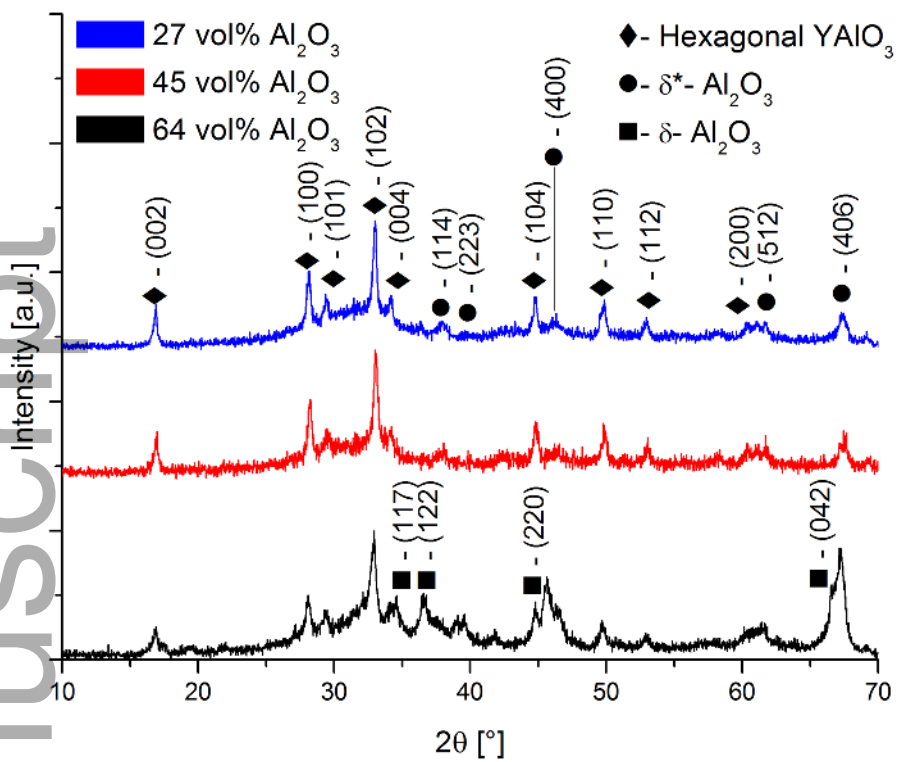
jace\_14980\_f4a.tif

Author Manuscript

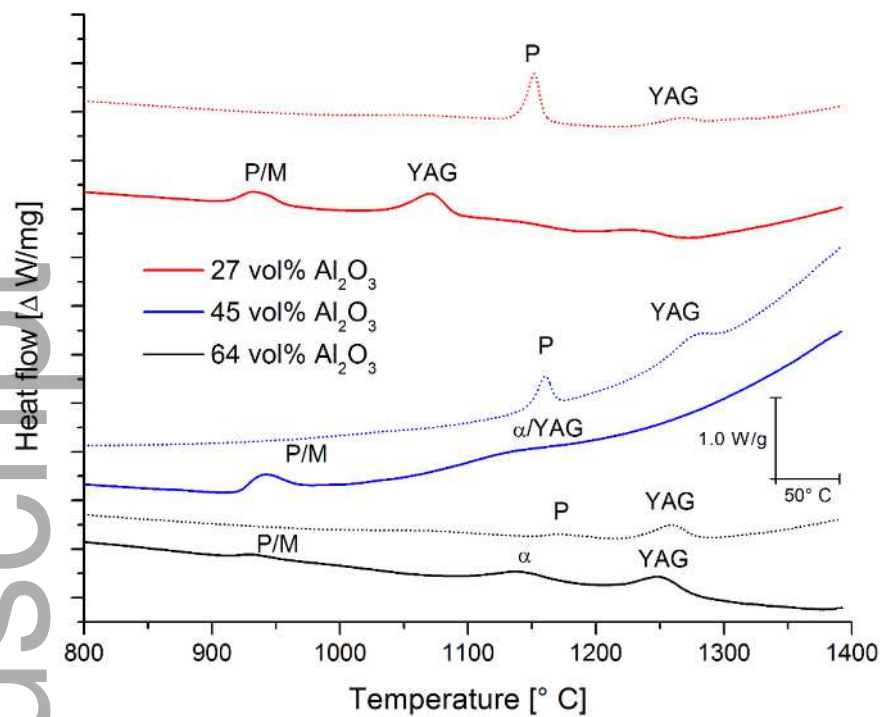




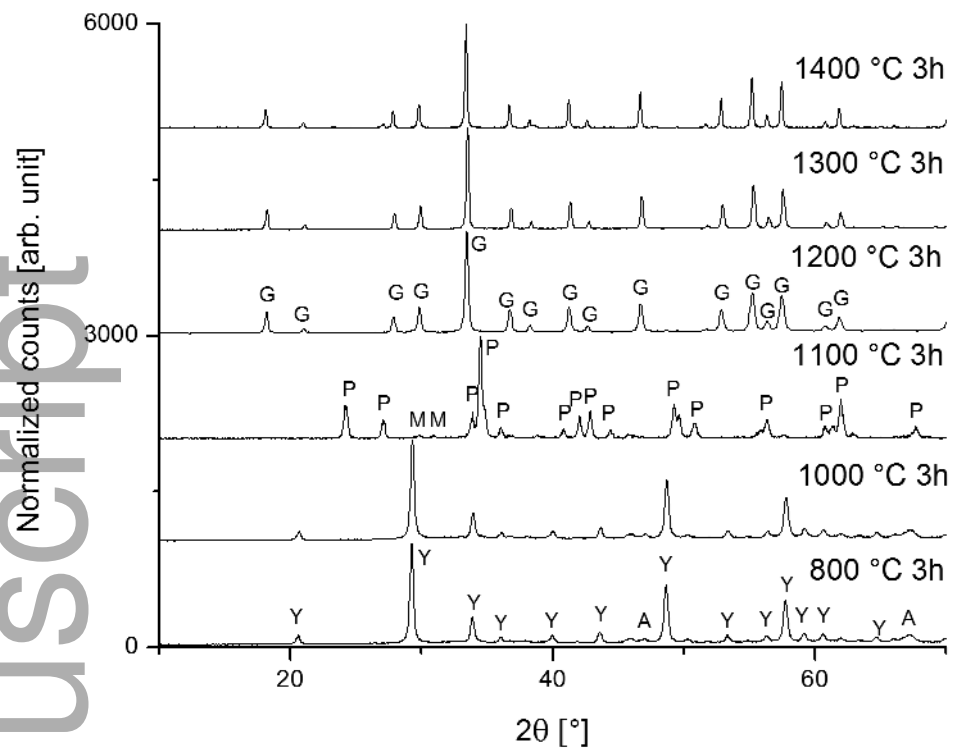
jace\_14980\_f5.tif



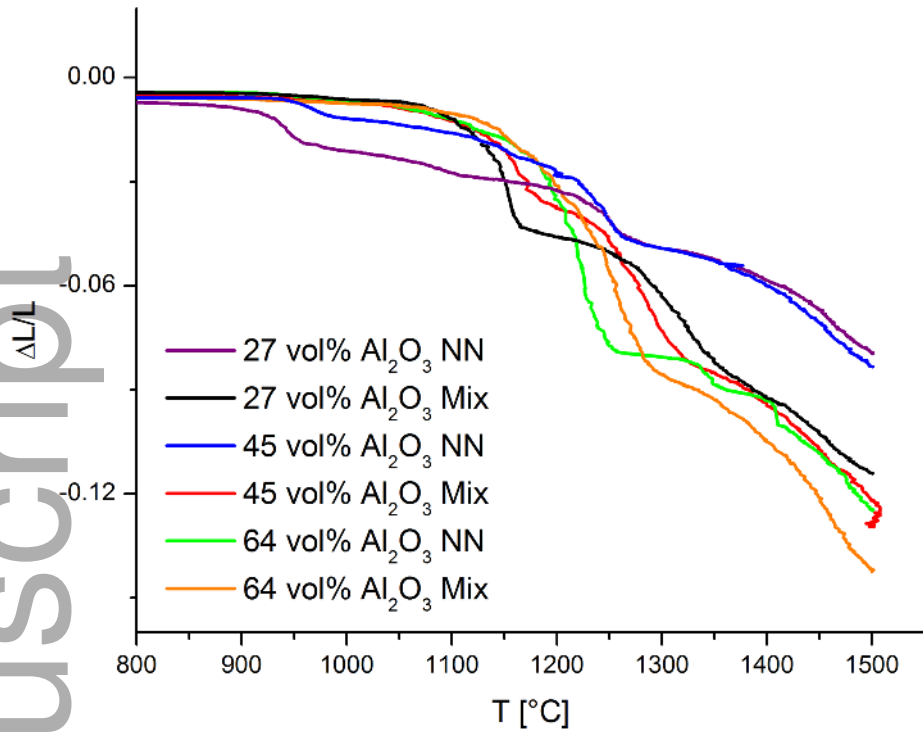
jace\_14980\_f6.tif



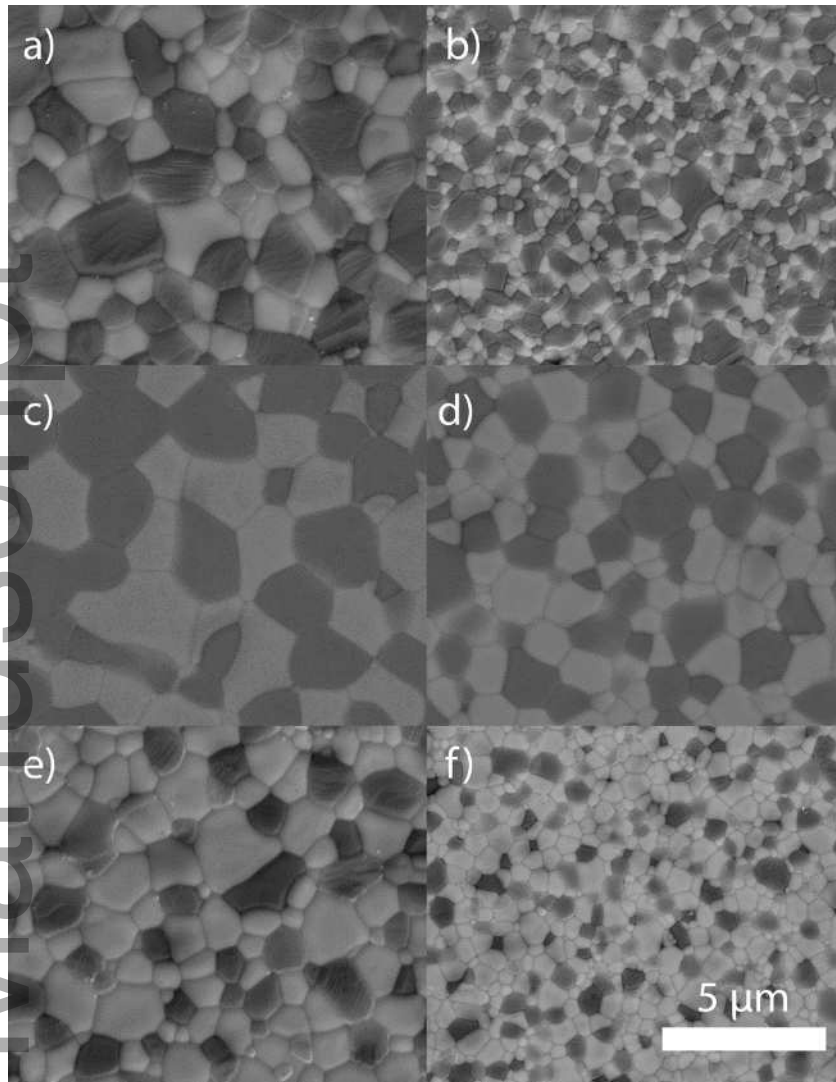
jace\_14980\_f7.tif



jace\_14980\_f8.tif



jace\_14980\_f9.tif



jace\_14980\_f10.tif